

Article

Adsorption and Desorption Behavior and Mechanism of Ruthenium in Nitrite–Nitric Acid System

Cong Li ¹, Chao Xie ^{1,2,3}, Tianjiao Jiang ^{1,3,*}, Lifeng Chen ^{1,3}, Shunyan Ning ^{1,3} , Caiwu Luo ^{2,3}, Qi Zheng ¹, Ji Wang ^{1,3} and Yuezhou Wei ^{1,3,4} ¹ School of Nuclear Science and Technology, University of South China, Hengyang 421001, China² School of Resources Environment and Safety Engineering, University of South China, Hengyang 421001, China³ Key Laboratory of Advanced Nuclear Energy Design and Safety, Ministry of Education, University of South China, Hengyang 421001, China⁴ School of Nuclear Science and Engineering, Shanghai Jiao Tong University, Shanghai 200240, China

* Correspondence: jiangtianjiao@usc.edu.cn

Abstract: Ruthenium is required to separate from high-level liquid waste (HLLW) because Ru is a valuable resource and is negatively influential on the vitrification process of HLLW. However, the separation of Ru is very challenging due to its complicated complexation properties. In this study, the adsorption and desorption characteristics of ruthenium on a synthesized SiPyR-N3 (weak-base anion exchange resin with pyridine functional groups) composite were investigated in nitric acid and nitrite–nitric acid systems, respectively, and the adsorption mechanism was explored. The experimental results showed that SiPyR-N3 has a significantly better adsorption effect on Ru in the nitrite–nitric acid system than in the nitric acid system, with an increase in the adsorption capacity of approximately three times. The maximum adsorption capacity of Ru is 45.6 mg/g in the nitrite–nitric acid system. The SiPyR-N3 possesses good adsorption selectivity ($SF_{\text{Ru/other metal ions}}$ is around 100) in 0.1 M NO_2^- –0.1 M HNO_3 solution. The adsorption processes of Ru in the two different systems are fitted with the pseudo-second-order kinetic model and Langmuir model for uptake kinetics and adsorption isotherms, respectively. The results obtained from the FT-IR, XPS, and UV absorption spectrometry indicate that NO_2^- was involved in the adsorption process either as a complexing species with the metal ions or as free NO_2^- from the solution. A 0.1 M HNO_3 + 1 M thiourea mixed solution shows effective desorption performance, and the desorption efficiency can reach 92% at 328 K.

Keywords: ruthenium; adsorption; high level liquid waste; nitrite–nitric acid system

Citation: Li, C.; Xie, C.; Jiang, T.; Chen, L.; Ning, S.; Luo, C.; Zheng, Q.; Wang, J.; Wei, Y. Adsorption and Desorption Behavior and Mechanism of Ruthenium in Nitrite–Nitric Acid System. *Toxics* **2024**, *12*, 181. <https://doi.org/10.3390/toxics12030181>

Academic Editor: Tiziana Missana

Received: 28 January 2024

Revised: 23 February 2024

Accepted: 25 February 2024

Published: 27 February 2024



Copyright: © 2024 by the authors. Licensee MDPI, Basel, Switzerland. This article is an open access article distributed under the terms and conditions of the Creative Commons Attribution (CC BY) license (<https://creativecommons.org/licenses/by/4.0/>).

1. Introduction

Nuclear energy is clean, safe, and highly efficient and thus provides a promising source of energy. Therefore, it plays a key role in the development of energy strategies for carbon neutralization with the lowest hazardous emissions to the environment [1]. Considering the rapid growth of nuclear energy, it has been expected that about 3200 t of spent nuclear fuel will be produced solely in China by the year 2030 [2]. Therefore, treatment of the generated spent nuclear fuel is important. Presently, the PUREX process is found to be an effective method for the separation and recovery of uranium (U) and plutonium (Pu) from spent nuclear fuel, resulting in high-level liquid waste. However, since other fission products (FPs), such as cesium, strontium, the platinum group metals (ruthenium, palladium, and rhodium), and minor actinides (MAs), which are intensely radioactive, remain in the HLLW, further treatment of HLLW is significantly important for the minimization of radiotoxicity to the environment [3].

Ru can be in various coordination complex forms and also in a variety of oxidation states [4]. ^{106}Ru with the half-life ($T_{1/2} = 373.6$ d) is one of the extremely difficult radionu-

clides to treat in all fission products [5]. Ru is mainly in the form of $\text{Ru}(\text{NO})^{3+}$ in the nitric acid solution of spent nuclear fuel, and once it is formed, it is difficult to change by substitution or oxidation–reduction reactions. In addition, $\text{Ru}(\text{NO})^{3+}$ easily forms more stable complexes with various ligands (such as NO_3^- , NO_2^- , etc.); hence, Ru is rather difficult to remove during the reprocessing of spent nuclear fuel. Considering the difficulty of Ru removal in a timely fashion, there are a number of drawbacks, namely, (1) in the PUREX process, part of Ru ($[\text{RuNO}(\text{NO}_3)_3(\text{H}_2\text{O})_2]$) is co-extracted with U and Pu by tributyl phosphate (TBP), but it is difficult to back-extract, which negatively affects the decontamination of U and contaminates subsequent products; (2) Ru is easily oxidized into volatile RuO_4 in the process of nuclear waste disposal, and then it causes the contamination area for RuO_4 recondensation to expand when it comes into contact with the cold tube walls; and (3) in the vitrification process, Ru, which is insoluble in borosilicate glass, is precipitated in the molten body as RuO_2 and a Pd–Ru–Te alloy and accumulates at the bottom of the melting furnace, which leads to an electrode short circuit and shortens the lifespan of the furnace [6]. On the other hand, Ru is an important strategic resource and an essential material in the fields of aerospace, catalysts, and electroplating [3]. However, the average abundance of Ru in the Earth's crust is only 0.001 ppm [7]. Fortunately, it has been anticipated that 2000 tons of Ru will be present in the spent nuclear fuel used by the world by the year 2030, which is about 62% of the mineral reserves [3]. Therefore, the secondary recovery of Ru from HLLWs has the ability to optimize the PUREX process and also recycle and reuse resources, which could solve the imbalance ratio between the supply and demand of Ru resources in both scientific and industrial applications.

HLLW has extremely strong radioactivity and high acidity, and the Ru morphologies are diverse, which poses extreme challenges in the separation of Ru from nuclear waste. Currently, the widely used methods are photoreduction [8], solvent extraction [9], ion exchange [10], electrochemical techniques [11–13], and adsorption [14–16]. Among these separation methods, the advantages of the ion exchange method are high selectivity, excellent adsorption properties for rare and precious metal ions (PGMs), simple operation, and strong regenerative ability. This method tends to be more favorable among researchers in the field of radioactive nuclide removal and separation. Previously, Lee et al. [17] investigated the adsorption effects of three types of ion exchange resins (IRN 78, Dowex 1 × 8 – 400, and AR-01) on Ru and Pd from simulated radioactive waste, and it was found that these resins have better adsorption for Pd than Ru. In another study, Suzuki et al. [18] found the adsorption ability was in the order of Pd > Rh > Ru on an N,N,N-trimethylglycine functionalized styrene–divinylbenzene copolymer (AMP 03) in a 0.1 M HNO_3 system. The traditional ion exchange materials have a good separation effect of Pd; however, the adsorption of Ru has slow kinetics and poor selectivity. Our group has been studying large pore (pore size 50–500 nm) SiO_2 -based ion exchange resins and SiO_2 -based extraction resins [19], which combine the high selectivity and good efficiency of organic extractants and organo-functional groups and the good stability of SiO_2 . These synthesized materials have been used for the separation of different radionuclides from HLLW, revealing excellent separation performance [20].

In addition, HLLW generally contains a high concentration of nitric acid (3–4 M) and a certain amount of nitrite resulting from nitric acid radiolysis and NO_3^- reduction in valence adjustment. The complexes formed by $[\text{RuNO}]^{3+}$ with NO_2^- tend to be much more stable than those formed with NO_3^- [21]. Therefore, the existence of nitrite has a significant influence on the adsorption efficiency of Ru [4]. However, there are currently very limited studies on the influence of nitrite on the species distribution of Ru, the use of nitrite in the auxiliary extraction of metal ions in the ion exchange system, and the in-depth exploration of the adsorption behavior and the adsorption mechanism of Ru.

Therefore, in this work, the adsorption behavior and mechanism of silica-based resins (SiPyR-N3) for Ru were investigated in nitrite–nitric acid systems. The sorption properties of Ru(III) ions in different nitric acid and nitrite concentrations were explored. The sorption properties were examined with different reaction times, initial metal ion concentrations,

sorption temperatures, and coexisting ions (to investigate the selectivity of multicomponent solutions) to determine their effects on adsorption performance. In addition, the adsorption mechanism of SiPyR-N3 towards Ru was also explored. After that, the elution behavior of adsorbed Ru was investigated using different reagents.

2. Materials and Methods

2.1. Reagents

Porous SiO₂ (average diameter of 75–150 μm) was purchased from Fuji Silysia Chemical Ltd., Kasugai, Japan. Ru(NO)(NO₃)_x(OH)_y (x + y = 3, analytical grade, 1.5 wt.% Ru), 4-vinylpyridine (4-VP, purity 95%), divinylbenzene (DVB, purity 55%), and nitrile-based cyclohexane (V-40, purity 98%) were purchased from Macklin Biochemical Technology Co., Ltd., Shanghai, China (www.macklin.cn, accessed on 20 February 2024). All the other reagents, such as nitric acid, hydrochloric acid, methanol, diethyl phthalate (DEP), azobisisobutyronitrile (AIBN), and acetophenone (ACP), were analytical grade and purchased from Sinopharm Chemical Reagent Co., Ltd., Shanghai, China (www.reagent.com.cn, accessed on 20 February 2024). All the solutions in the present experiment were prepared with ultrapure water.

2.2. Synthesis of Materials

SiPyR-N3 was described as a kind of pyridine-type weakly basic anion exchange resin obtained through a one-pot copolymerization reaction using 4-vinylpyridine (as a monomer) and divinylbenzene (as a crosslinking agent). The preparation of this material was previously reported in our work [22]. In detail, 6.41 mL of DVB, 17.69 mL of 4-VP, 45 mL of ACP, 30 mL of DEP, 0.3215 g of AIBN, and 0.2144 g of V-40 were mixed thoroughly. Then, the mixed solution was suctioned into the rotary evaporator using a reverse suction method under vacuum conditions and was put in full contact with 100 g of SiO₂. The oil phase gradually entered the pores of the SiO₂ substrate through capillary action. After sufficient mixing, nitrogen gas was injected to restore the inside of the flask to normal pressure, and the temperature was gradually changed for heating [23]. The chemical structure and photograph (of the powder form) of SiPyR-N3 are shown in Figure 1a,b, respectively.

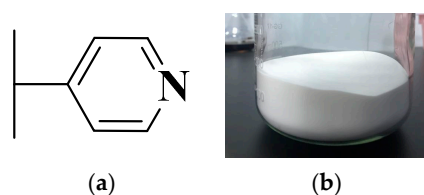


Figure 1. (a) Skeletal structure of SiPyR-N3 and (b) photograph of SiPyR-N3 powder.

The synthesis route is shown in Figure 2 [23].

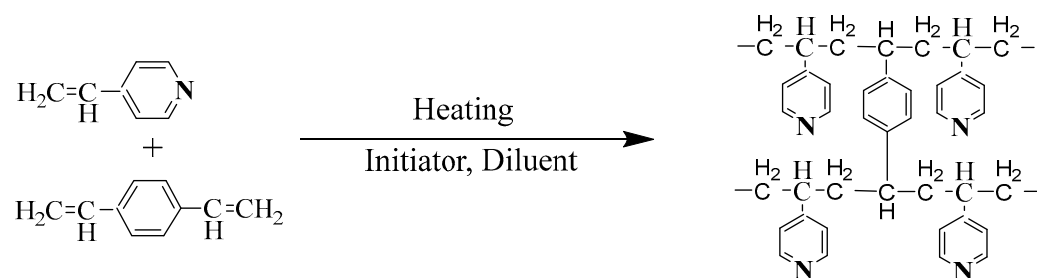


Figure 2. SiPyR-N3 synthesis route.

2.3. Adsorption Experiments

Batch adsorption was used to evaluate the adsorption and desorption performance of the prepared SiPyR-N3 for Ru ions. The experiment was conducted in a glass bottle with a screw cap at 0.02 g mL⁻¹ solid–liquid ratio, followed by mechanical oscillation at a constant speed of 160 revolutions per minute (RPM). After solid–liquid separation using a filter membrane (1.2 mesh), the concentrations of Ru and other metal ions were determined by an inductively coupled plasma spectrometer (ICP-AES). The adsorption capacity Q (mg·g⁻¹), adsorption efficiency E (%), distribution coefficient K_d (mL g⁻¹), and separation factor $SF_{A/B}$ toward Ru were calculated, as shown in Equations (1)–(4).

$$Q = \frac{(C_0 - C)}{m} \times V, \quad (1)$$

$$E = \frac{(C_0 - C)}{C_0} \times 100\%, \quad (2)$$

$$K_d = \frac{(C_0 - C)}{C} \times \frac{V}{m}, \quad (3)$$

$$SF_{A/B} = K_{dA} / K_{dB}, \quad (4)$$

where C_0 and C represent the concentration of Ru in the solution before and after adsorption, respectively. Furthermore, V and m represent the volume of the Ru initial solution and the mass of the adsorbent, respectively.

2.4. Desorption Procedure

Desorption should also be considered in practical applications, as it is considered an important parameter for the evaluation of adsorbent performance. The effects of desorption agents, desorption time, and temperature on the desorption rate were studied. SiPyR-N3 after static adsorption (V/m : 5 mL/0.1 g, [metal ions]: 2 mmol L⁻¹, time: 24 h, temperature: 298 K, [HNO₃]: 0.1 mol L⁻¹, [NaNO₂]: 0.1 mol L⁻¹) was washed with ultrapure water until the filtrate pH was constant and separated using a Brinell funnel; then, it was put into a vacuum dryer, before being used for subsequent desorption experiments. The static desorption experiment was conducted in a constant-temperature water bath. The desorption performance was evaluated by calculating the desorption quantity Q_d (see Equation (5)) and the desorption efficiency E_d (see Equation (6)) based on the measured Ru concentration.

$$Q_d = C_d \times \frac{V}{m}, \quad (5)$$

$$E_d = \frac{Q_d}{Q} \times 100\%, \quad (6)$$

where Q_d and Q (mg·g⁻¹) are the desorption quantity and the adsorption capacity of Ru by a gram of resin, and C_d represents the concentration of Ru in the solution after elution. V and m , respectively, represent the volume of the eluting agent and the mass of SiPyR-N3 after adsorption.

2.5. Adsorption Mechanism Study

In order to study the type of binding on the SiPyR-N3 surface and the subsequent adsorption mechanism, FT-IR (IRTracer-100, SHIMADZU; Kyoto, Japan) was employed to detect the functional groups of the material after treatment with nitric solution and the nitrite and nitric mixture. In detail, these samples were firstly dried at 60 °C before being ground with KBr (at a mass ratio of 100:1: w/w) and then pressed into a KBr disc. Furthermore, UV spectroscopy (UV-600 Plus, SHIMADZU; Kyoto, Japan) was applied to analyze Ru species in the NaNO₂-HNO₃ solution. The absorption spectra of the metal ions in different concentrations of NaNO₂ solutions were measured in the wavelength range of 300 to 450 nm. In detail, a mixture of different concentrations of NaNO₂ and ruthenium was

diluted 10 times, and a corresponding concentration of NaNO_2 solution was selected for the blank sample to determine the mixed solution absorbance. SEM (Hitachi Regulus8100, HITACHI; Tokyo, Japan) was used for studying the morphological structure of the surface. The chemical composition and the elemental contents were detected using EDS (Ultima Expert, Kyoto, Japan). XPS (Thermo ESCALAB 250 XI, THERMO FISHER; New York, NY, USA) analysis was used. The survey spectra were obtained for the global identification of the main elements, in which the core levels (signal deconvolution) were adjusted after calibration of the binding energy (BE, eV).

3. Results and Discussion

3.1. Evaluation of Adsorption Performance

3.1.1. Effects of HNO_3 , NaNO_2 , and NaNO_3 Concentration

Figure 3 shows the effect of nitric acid concentration on the K_d of Ru. The adsorption results of Ru by SiPyR-N3 with weak base groups showed that the K_d decreased significantly with the increase in HNO_3 concentration, and the K_d of Ru dropped from 19.4 mL/g to 1.1 mL/g in the range of 0.1–3 M HNO_3 . The reason may be that a high H^+ concentration inhibits the deprotonation and ion exchange capacity of the adsorbent, which enhances the repulsion force with the protonated quaternary amine groups on the resins and decreases the adsorption with Ru species (Figure S1), so the adsorption decreased with nitric acid concentration [22].

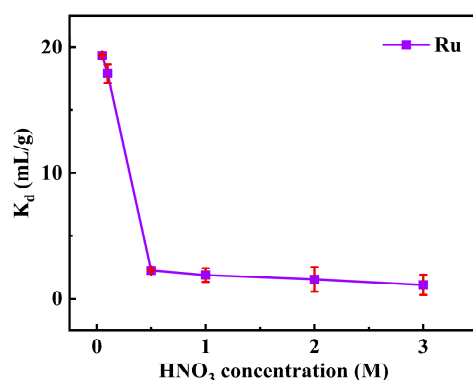


Figure 3. Effect of initial HNO_3 concentration on adsorption of Ru ($m/V = 0.02 \text{ g mL}^{-1}$, $C_{\text{Ru}} = 2 \text{ mmol L}^{-1}$, $T = 298 \text{ K}$).

Figure 4 shows the effect of the NaNO_2 and NaNO_3 concentration on the adsorption of Ru. Interestingly, the K_d and the adsorption capacity increased significantly with the increase in NaNO_2 concentration (Figure S2). The maximum K_d reaches 311 mL/g in 0.1 M HNO_3 -0.3 M NO_2^- . It is possible that different concentrations of NO_2^- and NO_3^- coordinate with $[\text{RuNO}]^{3+}$ to form a variety of Ru nitrite complexes, such as $\text{RuNO}(\text{NO}_2)(\text{NO}_3)_2(\text{H}_2\text{O})_2$, etc. [24]. When the concentration of NaNO_2 increased above 0.3 M, the adsorption capacity slightly decreased, which may be due to the competitive adsorption between the excess NO_2^- and ruthenium complexes. For 0.1 M NaNO_2 , the K_d reached 270 mL/g. Because of the suitable difference in the K_d values in 0.1 M and 0.3 M NaNO_2 solutions and the slight differences in the adsorption efficiency and adsorption capacity (Figure S1), additionally, the redox reaction was performed between nitric acid (strong oxidizing agent) and sodium nitrite, a more stable 0.1 M NaNO_2 system was selected for subsequent adsorption experiments. In addition, the effect of the NaNO_3 concentration on the adsorption of Ru was also studied. As shown in Figure 4, the adsorption effect gradually deteriorates as the concentration of NO_3^- increases. In nitric acid solution, Ru forms nitrate–water complexes ($\text{Ru}(\text{NO})(\text{NO}_3)_x(\text{H}_2\text{O})_{5-x}]^{3-x}$). With the increase in the nitric acid concentration, the chemical species ($\text{Ru}(\text{NO})(\text{NO}_3)_3(\text{H}_2\text{O})_2$, $[\text{Ru}(\text{NO})(\text{NO}_3)_4\text{H}_2\text{O}]^-$, $[\text{Ru}(\text{NO})(\text{NO}_3)_5]^{2-}$, and $[\text{Ru}(\text{NO}_3)_6]^{4-}$) of Ru change as follows:

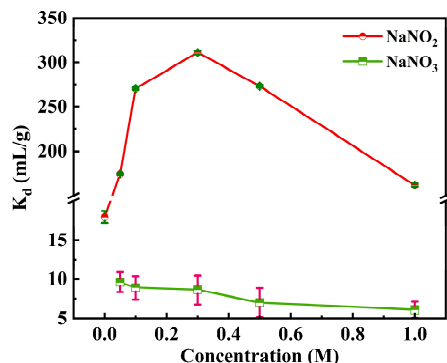
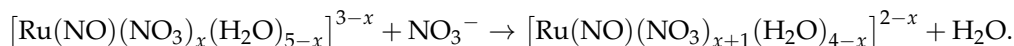


Figure 4. Effect of initial NaNO₂ and NaNO₃ concentration on adsorption ($m/V = 0.02 \text{ g mL}^{-1}$, $C_{\text{Ru}} = 2 \text{ mmol L}^{-1}$, $C_{\text{HNO}_3} = 0.1 \text{ mol L}^{-1}$, $T = 298 \text{ K}$).

Therefore, as the concentration of nitrate increases, more active sites are needed for ion exchange and adsorption with $\text{Ru}(\text{NO})^{3+}$. According to the different adsorption properties in NO_2^- and NO_3^- systems, it is deduced that the Ru species formed in the NO_2^- solution are more stable and easily adsorbed by SiPyR-N3 [25].

3.1.2. Kinetics Studies

The adsorption kinetics of Ru on SiPyR-N3 in 0.1 M HNO₃ solution and 0.1 M HNO₃-0.1 M NaNO₂ solution at different temperatures were studied, respectively. Firstly, it is observed from Figure 5a that the adsorption equilibrium was reached at 24 h in the 0.1 M HNO₃ solution. As the temperature increases, the adsorption capacity slightly increases, indicating that the adsorption process is endothermic. Figure 5c shows the effects of temperature and time on the adsorption of Ru in the nitrite–nitric acid system. The adsorption equilibrium was reached after 12 h, which is nearly one times faster than that in the nitric acid system. Furthermore, the adsorption capacity at 298 K was 8.5 mg/g, which is four times more than that in NO_3^- , and it increased slightly with the increase in temperature. Comparing these results with those obtained from 0.1 M HNO₃ on Ru adsorption by SiPyR-N3, the adsorption rate and adsorption capacity were significantly increased, and the K_d of Ru increased by 15 times in 0.1 M NaNO₂-0.1 M HNO₃. The experimental results show that the addition of NaNO₂ is beneficial to the adsorption of Ru on SiPyR-N3. As the temperature increased from 298 K to 318 K, the adsorption capacity of SiPyR-N3 for Ru increased from 8.57 mg/g to 9.18 mg/g, indicating that the reaction is an endothermic process.

The adsorption kinetics were further analyzed by the pseudo-first-order kinetics equation (PFORE, Equation (7)) and pseudo-second-order kinetics equation (PSORE, Equation (8)):

$$\ln(Q_e - Q_t) = \ln Q_e - k_1 t, \quad (7)$$

$$\frac{t}{Q_t} = \frac{1}{k_2 Q_e^2} + \frac{t}{Q_e}, \quad (8)$$

where Q_t is the adsorption capacity at t (h), Q_e (mg g^{-1}) is the adsorption capacity at equilibrium, and k_1 (h^{-1}) and k_2 ($\text{mg g}^{-1} \text{ h}^{-1}$) are the constants of the PFORE and PSORE, respectively.

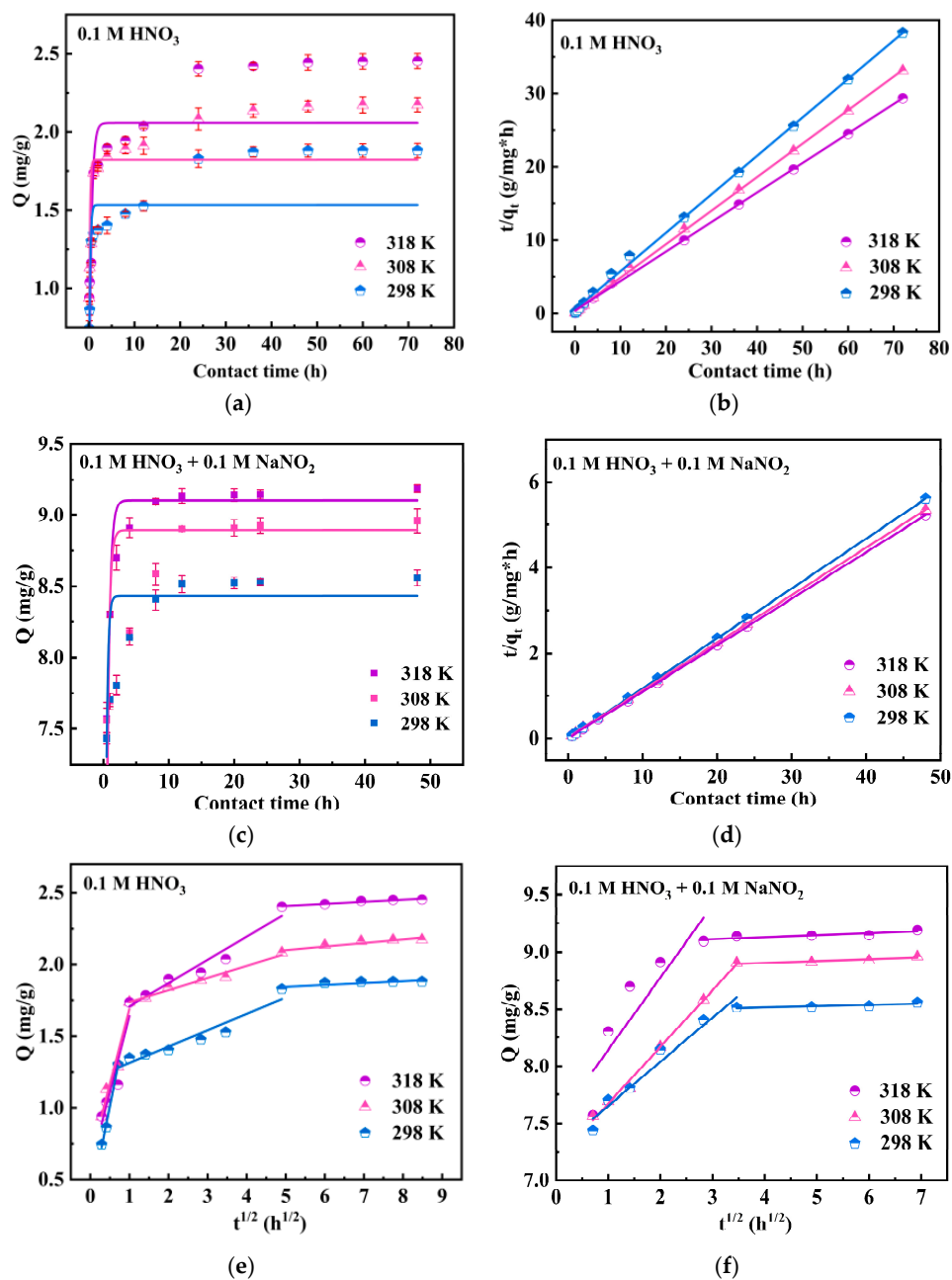


Figure 5. Pseudo-first-order kinetic fitting (a) and pseudo-second-order kinetic fitting (b) of Ru in nitric acid system. Pseudo-first-order kinetic fitting (c) and pseudo-second-order kinetic fitting (d) of Ru in the nitrite–nitric acid system. Internal particle diffusion model in nitric acid system (e) and in the nitrite–nitric acid system (f). ($m/V = 0.02 \text{ g mL}^{-1}$, $C_{\text{Ru}} = 2 \text{ mmol L}^{-1}$, $C_{\text{HNO}_3} = 0.1 \text{ mol L}^{-1}$, $C_{\text{NaNO}_2} = 0.1 \text{ mol L}^{-1}$).

The fitting results are shown in Figure 5 and Table S1. In both systems, the PSORE showed a better fitting of the experimental data than the PFORE, and its correlation coefficient (R^2) was closer to 1. In addition, the calculated Q_e value of the pseudo-second-order kinetics model had excellent consistency with the actual adsorption equilibrium capacity ($Q_{e,exp}$). Because the pseudo-second-order model is more suitable for describing the ruthenium adsorption process, it is indicated that the adsorption reaction of Ru on SiPyR-N3 is chemisorption.

In order to further determine the control steps of the adsorption rate, the intraparticle diffusion equation was used for fitting (Equation (9)). The transfer of adsorbed substances

during solid–liquid adsorption can be characterized as boundary layer diffusion or intraparticle diffusion.

$$Q_t = k_i t^{1/2} + C, \quad (9)$$

where Q_t (mg g^{-1}) is the adsorption capacity at time t (h), k_i is the intraparticle diffusion constant, and C is an arbitrary constant that represents the thickness (or resistance) of the boundary layer.

In particular, the intraparticle diffusion model was fitted for both systems (Figure 5e,f). The trilinear and bilinear regions were investigated for the nitric acid and the nitrite–nitric acid systems, respectively, indicating that both belong to a multistep adsorption mechanism throughout the entire process. In both systems, the slope of step 1 is greater than that of step 2. As the adsorption reaction proceeded, the following steps tended to the adsorption equilibrium, indicating it was not a restricting step for Ru adsorption. Moreover, the fitting curves of both systems do not pass through the origin, inferring that the adsorption includes intradiffusion and chemisorption, and its rate is controlled by chemisorption. The differences in the linear region between the two may be due to the addition of nitrite. The slope of step 1 increased with the increase in temperature, indicating that the SiPyR-N3 material has a faster reaction rate for Ru adsorption at higher temperatures.

3.1.3. Isotherm Studies

Figure 6a,b show the relationship between the adsorption capacity and the initial concentration of Ru in the nitric acid system and the nitrite–nitric acid system, respectively. Firstly, in the HNO_3 solution, the adsorption capacity of SiPyR-N3 increased as the concentration of Ru increased before it reached saturation, and it increased with the temperature but just from 9.8 mg/g to 11.9 mg/g, which indicated that the adsorption capacity of materials for Ru is limited in a nitric acid system and the increase in temperature is marginally helpful for adsorption. Although the adsorption capacity is increased by 21% with the temperature, it is still too small and cannot reach the desired efficiency. Secondly, in the $\text{HNO}_3\text{-NO}_2^-$ solution, the adsorption capacity of SiPyR-N3 for Ru also follows the pattern of a steep increase, then saturation, and then stabilization. The maximum adsorption capacity of SiPyR-N3 for Ru was 30.5 mg/g at 298 K in the $\text{HNO}_3\text{-NO}_2^-$ system, almost three times more than that in the HNO_3 system. It indicated that nitrite enhances the adsorption affinity. Furthermore, the saturated adsorption capacity significantly increased from 30.5 mg/g to 45.6 mg/g with the increase in temperature from 298 K to 318 K. Two isotherm models are used to fit the experimental data, namely, the Langmuir isotherm model (associated with monolayer adsorption, without any interactions of the adsorbed molecules; homogeneous adsorption) (Equation (10)) and the Freundlich isotherm model (multilayer sorption with possible interactions of the adsorbed molecules; heterogeneous distribution of the adsorption energies) (Equation (11)).

$$Q_e = \frac{q_m \times K_L \times C_e}{1 + K_L \times C_e}, \quad (10)$$

$$Q_e = K_F \times C_e^{\frac{1}{n}}, \quad (11)$$

where Q_e (mg g^{-1}) is the equilibrium uptake amount, and q_m (mg g^{-1}) and C_e (mg L^{-1}) are the calculated saturation adsorption capacity and equilibrium ion concentration in solution, respectively. K_L (L mg^{-1}) is the Langmuir constant, and K_F ($\text{mg}^{1-n} \text{L}^n \text{g}^{-1}$) and n are the Freundlich constants.

The fitting parameters are shown in Table S2. The correlation coefficients (R^2) of the Langmuir isotherm mode under both systems are higher than 0.95; meanwhile, they are also exposed to different temperatures. Obviously, the Langmuir model had a higher fitting coefficient than the Freundlich model in both systems. Therefore, the Langmuir model exhibits a better description of the Ru adsorption process. The fitted Q_m values are very close to the experimental ($Q_{e,exp}$) values (with errors of less than 5%). Hence, it

can be speculated that the adsorption process of Ru on SiPyR-N3 is mainly monolayer chemisorption.

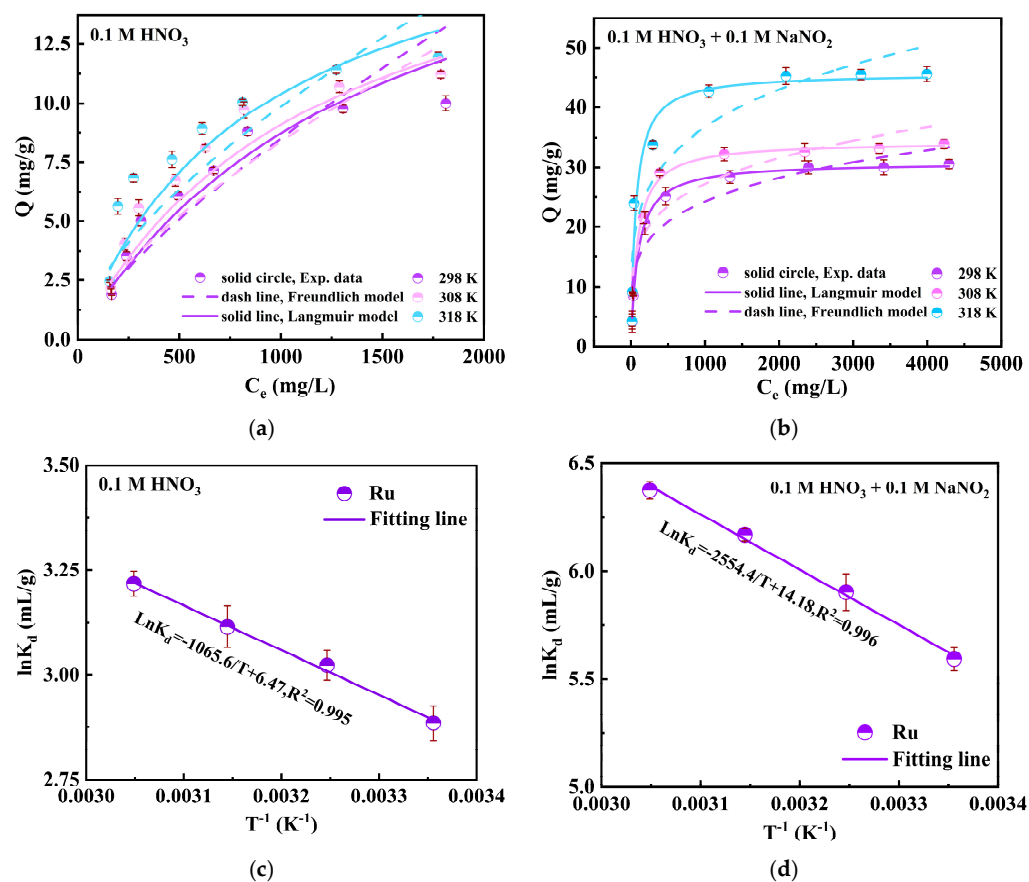


Figure 6. Adsorption isotherms of Ru in 0.1 M HNO₃ solution (a), adsorption isotherms of Ru in 0.1 M HNO₃ + 0.1 M NaNO₂ solution (b). Relationship diagram between $\ln K_d$ and T^{-1} of Ru in nitric acid system (c) and in the nitrite–nitric acid system (d). ($m/V = 0.02 \text{ g mL}^{-1}$, $C_{\text{HNO}_3} = 0.1 \text{ mol L}^{-1}$, $C_{\text{NaNO}_2} = 0.1 \text{ mol L}^{-1}$).

3.1.4. Adsorption Thermodynamics

The adsorption thermodynamics are shown in Figure 6c,d and Table S3. Based on kinetic and isotherm results, the adsorption capacity increased with increasing temperature. The main thermodynamic parameters can be obtained based on the van 't Hoff equation [26–29]:

$$\ln K_d = -\frac{\Delta H^\circ}{RT} + \frac{\Delta S^\circ}{R}, \quad (12)$$

$$\Delta G^\circ = \Delta H^\circ - \Delta S^\circ T, \quad (13)$$

where ΔG° (J mol^{-1}), ΔH° (J mol^{-1}), and ΔS° ($\text{J K}^{-1} \text{ mol}^{-1}$) are the changes in the Gibbs free energy, enthalpy, and entropy, respectively. R ($8.314 \text{ J K}^{-1} \text{ mol}^{-1}$) represents the gas constant at temperature T (K).

As shown in Table S3, the values of ΔH° and ΔS° are positive, while ΔG° is negative, which indicates that the adsorption process is endothermic. This is consistent with the observation results of the experiment. The negative value of ΔG° indicates that adsorption is spontaneous. A positive ΔS° value indicates that the adsorption process is entropy-driven. The differences in parameters in both systems are mainly due to the diverse Ru complexes formed, which show different stability and affinity.

3.1.5. Adsorption Selectivity Experiment

The HLLW is characterized as very complex with multiple metal ions, such as Sm, Y, Ce, Pr, Gd, La, Eu, Nd, Zr, Sr, etc., except Ru. Therefore, in order to evaluate the selectivity of SiPyR-N3 for Ru in natural samples, the adsorption experiments on simulated HLLW were carried out in the $\text{HNO}_3\text{-NO}_2^-$ system. As shown in Figure 7, SiPyR-N3 exhibited poor adsorption of the coexisting metal ions except Zr. The K_d of Ru was as high as $207 \text{ g}\cdot\text{mL}^{-1}$ in the multiple metal ion mixed solution and was obviously higher than other metal ions ($K_{d(\text{Zr})} = 72 \text{ g}\cdot\text{mL}^{-1}$, $K_{d(\text{other metals})} < 1.2 \text{ g}\cdot\text{mL}^{-1}$). Furthermore, the $SF_{\text{Ru/other metal ions}}$ is greater than 99.8, except for $SF_{\text{Ru/Zr}}$, indicating that SiPyR-N3 has excellent adsorption performance and good selectivity for Ru. Partial Zr was adsorbed by SiPyR-N3 due to the strong affinity between Zr and N-containing groups [30]. Regarding Pd, which is also a platinum group metal, previous articles have reported relevant research [22]. Generally, SiPyR-N3 has good adsorption ability and selectivity for Ru in HLLW.

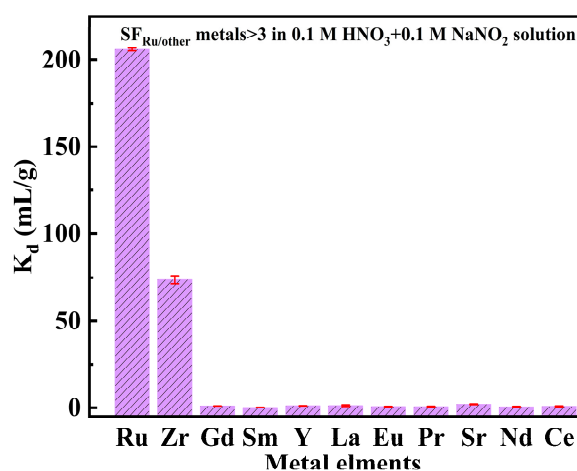


Figure 7. Distribution coefficients of typical metal elements in HLLW. ($m/V = 0.02 \text{ g mL}^{-1}$, $C_{[\text{metal ion}]} = 2 \text{ mmol L}^{-1}$, $C_{\text{HNO}_3} = 0.1 \text{ mol L}^{-1}$, $C_{\text{NaNO}_2} = 0.1 \text{ mol L}^{-1}$, $T = 298 \text{ K}$).

3.2. Interaction Mechanism Study

3.2.1. FT-IR Analysis

To confirm successive grafting and emphasize the changes that occurred in the functional groups before and after adsorption, SiPyR-N3 was characterized by FT-IR. As shown in Figure 8, the Si-O appeared with three identical peaks at around 1107 cm^{-1} (Si-O-Si bands overlapped with δ_{CH} (out-of-plane) [20]), 805 cm^{-1} (Si-O-Si bands, and the increase in the intensity after adsorption is mainly due to overlapping with NO_3^- from the solution), and 471 cm^{-1} (Si-O bands). The clear characteristic peak at 1385 cm^{-1} after adsorption of Ru by SiPyR-N3 is in connection with NO_3^- , indicating the involvement of NO_3^- in the adsorption process. The absorption peaks at 1458 cm^{-1} and 1631 cm^{-1} belong to the characteristic peaks of the pyridine ring with Si-OH for SiO_2 , and there is almost no change after adsorption. Moreover, a new absorption peak appeared at the position of 1872 cm^{-1} after adsorption. The weak peak at 2932 cm^{-1} belongs to alkyl C-H. The peak at 3449 cm^{-1} comes from the O-H bond of adsorbed H_2O .

3.2.2. UV Absorption Spectra Analysis

Figure 9 shows the UV absorption spectra of Ru in nitrite–nitric acid solution. Firstly, there are multiple obvious absorption peaks at 325–400 nm only in the case of the presence of nitrite [31]. In contrast, the spectral curve is smooth, and there are no absorption peaks without nitrite in the solution. In detail, in Figure 9 curves (1) to (3), nitrite has strong absorption peaks at 325–400 nm, while Ru has no absorption peak. In the 0.1 M NO_2^- – 0.1 M HNO_3 system (in Figure 9 curves (3) and (6)), the peaks between 325 and 400 nm

decreased significantly after adding Ru to the solution, which indirectly provides evidence of the formation of complexes between Ru and NO_2^- and exhibits the complexing ability of nitrite and ruthenium at different concentrations. In addition, although the intensity of these peaks decreased obviously, weak peaks between 325 and 400 nm with a certain regularity can still be observed. In detail, in Figure 9 curves (4) to (9), the UV spectral absorption peaks are ranked from strong to weak in the order (7) > (8) > (6) > (5) > (1), where the corresponding NaNO_2 concentration is 0.3, 0.5, 0.1, 0.05, and 1 M, respectively, which is consistent with the results of the batch adsorption experiments (Figure 4). In light of the above results, it can be speculated that the concentration of nitrite in solution decreases due to the formation of Ru–nitrite complexes ($[\text{RuNO}(\text{NO}_3)(\text{NO}_2)_2(\text{H}_2\text{O})_2]^{0}$, $[\text{RuNO}(\text{NO}_2)_2(\text{H}_2\text{O})_3]^+$, etc.), and the adsorption is better with the higher peaks in this work [25]. The degree of Ru complexation varies with the concentration of nitrite added, thereby affecting the adsorption effect of SiPyR-N3 on Ru.

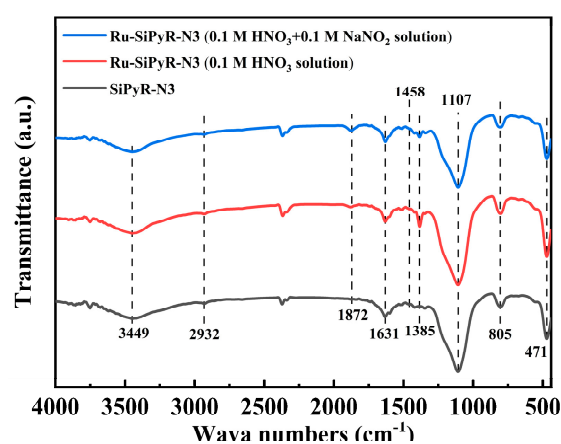


Figure 8. FT-IR spectra of fresh and Ru-loaded SiPyR-N3.

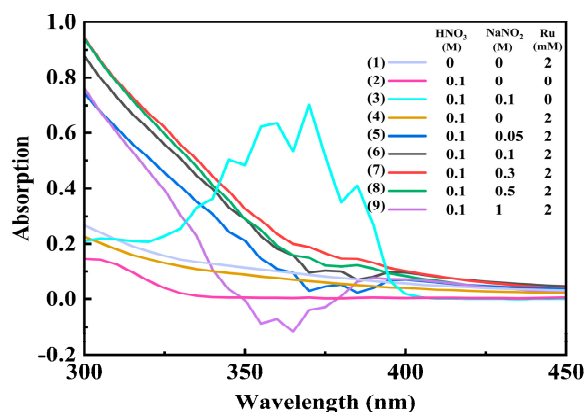


Figure 9. UV absorption spectrum of Ru in sodium nitrite solution.

3.2.3. SEM-EDS Analysis

Figure 10a,c,e show the SEM images of SiPyR-N3 before and after Ru adsorption. The adsorbent maintained the original size and morphological characteristics after adsorption, indicating that the material had good mechanical stability. Based on the elemental maps and the atomic proportions of C, N, O, Si, and Ru, it is further confirmed that Ru is successfully adsorbed. The amount of N and O increased significantly after adsorption, which may be due to the formation of Ru and nitrite complexes.

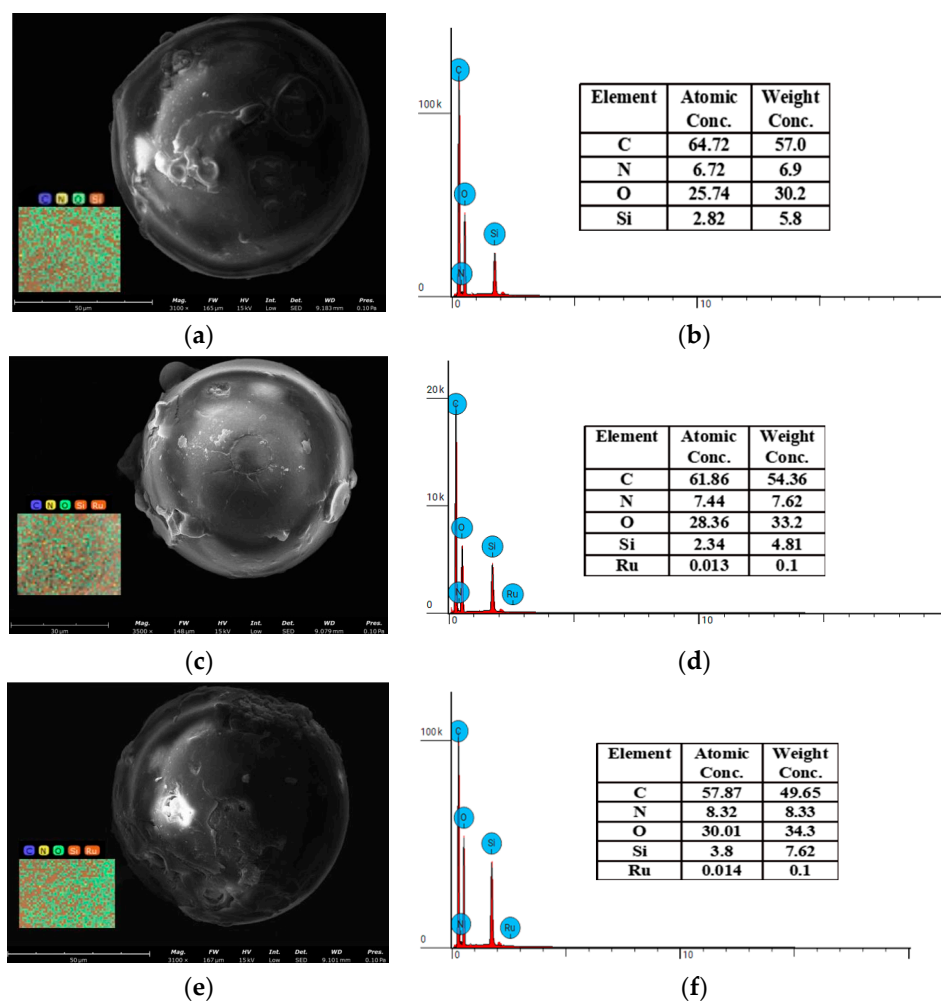


Figure 10. SEM-EDS characterization of SiPyR-N3 material (a,b) after adsorption in nitric acid system (c,d) and in the nitrite–nitric acid system (e,f).

3.2.4. XPS Analysis

In order to further investigate the Ru adsorption mechanism by SiPyR-N3, XPS analysis was used to identify the changes in chemical bonds of SiPyR-N3 after adsorption, as shown in Figure 11. The silica core is confirmed by signal Si 2p and Si 2s, while the organic support is identical through the presence of C 1s, O 1s, and N 1s. The presence of Ru is confirmed by signals Ru 3d and Ru 3p, which emphasize the successful adsorption of Ru. It was observed that the peak area of Ru 3p is bigger in the 0.1 M HNO₃-0.1 M NaNO₂ system than in the 0.1 M HNO₃ system, indicating a better adsorption performance. In addition, the change in N peak before and after adsorption was observed clearly. In detail, the N 1s spectrum of the pristine adsorbent SiPyR-N3 has two deconvoluting peaks at 398.98 and 400.68 eV, belonging to C–N and the tertiary amine on the pyridyl ring, respectively. In the HNO₃ system, these peaks shifted from 398.98 and 400.68 eV to 398.48 and 400.98 eV, respectively, after the adsorption of Ru, speculating that the complexation of pyridine–N with Ru affects the electronic chemical environment of N 1s. The new N 1s peaks at 405.68 eV are contributed by Ru–NO₃[−]. In the NaNO₂-HNO₃ system, the peaks of C–N, C=N, and Ru–NO₃[−] shifted after adsorption; furthermore, a new peak at 403.38 eV corresponds to M (Ru, Na)–NO₂, proving the complexations of Ru and nitrite are adsorbed on the SiPyR-N3 [32–37].

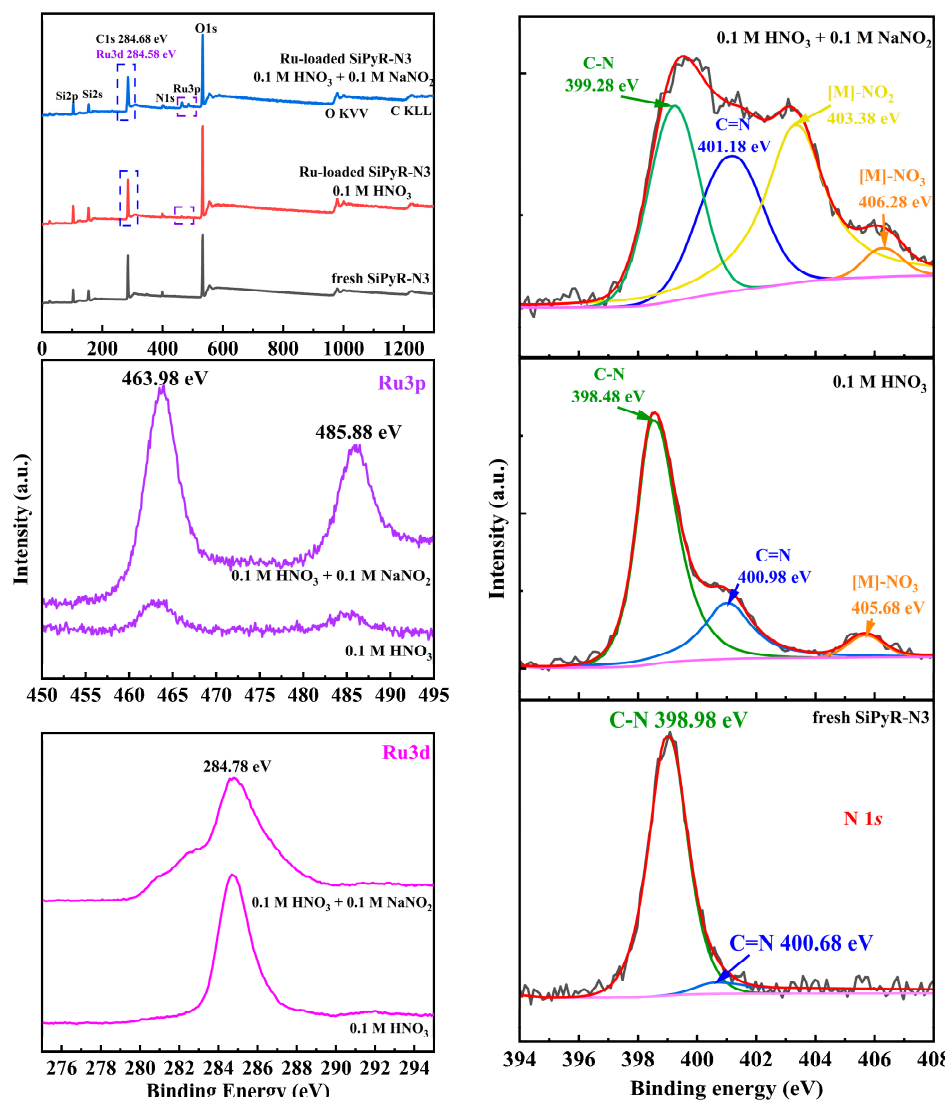


Figure 11. XPS survey scans of fresh SiPyR-N3 and Ru-loaded SiPyR-N3.

3.3. Desorption Behavior

Figure 12a shows the desorption efficiency of SiPyR-N3 loaded with Ru using different desorption agents. Five typical desorption agents were selected, including H₂O, 1 M oxalate, 10 M HNO₃, 0.1 M NH₄OH, and 0.1 M HNO₃ + 1 M thiourea. H₂O has almost no desorption effect on the adsorbed Ru, and the desorption efficiency of oxalate is also very weak. The desorption effect of HNO₃ and NH₄OH on Ru is not significantly different, with desorption efficiency of 14% and 15%, respectively. The 0.1 M HNO₃-1 M CH₄N₂S solution has the best desorption ability but only with the *E_d* of 30% at 298 K. The desorption results prove that Ru is mainly adsorbed by chemisorption in the NaNO₂-HNO₃ solution and is difficult to desorb. Further, the effect of temperature on the desorption efficiency was explored, as shown in Figure 12b. The increase in temperature could contribute much to improving the desorption efficiency, and the efficiency was basically unchanged above 328 K, so 328 K is the optimal desorption temperature. Since the *E_d* of 318 K reached 81%, the desorption kinetics of Ru were investigated at this temperature. As shown in Figure 12c, the desorption approaches equilibrium at 16 h.

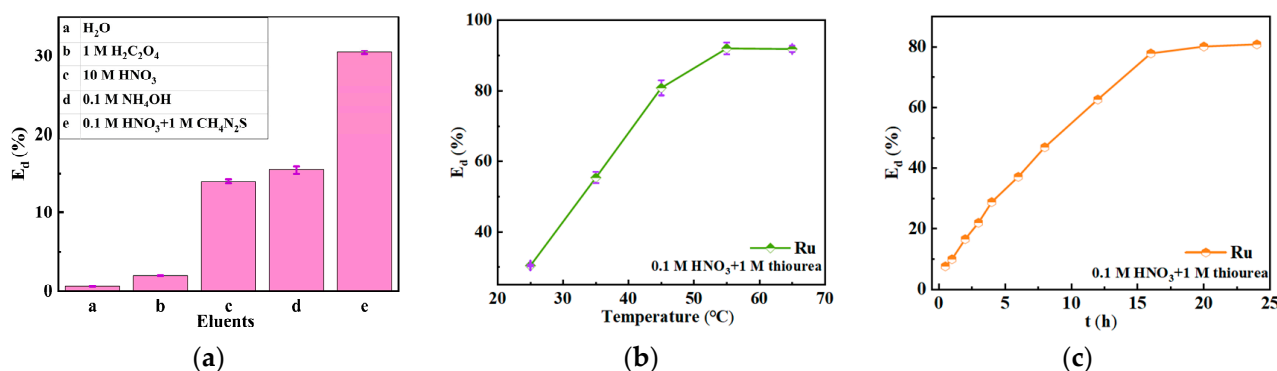


Figure 12. Desorption efficiency of ruthenium by different desorption agents at 298 K (a). Effect of temperature on desorption efficiency (b). Kinetic study on desorption process at 318 K (c). (Adsorption conditions: $Ru = 2 \text{ mmol L}^{-1}$, medium = 0.1 M HNO_3 -0.1 M $NaNO_2$, $m/V = 0.02 \text{ g mL}^{-1}$).

4. Conclusions

In this work, the adsorption and desorption behavior of Ru(III) with SiPyR-N3 adsorbent was systematically investigated in nitric acid and nitrite–nitric acid systems, respectively. The distribution coefficient of Ru was assigned to 270 mL/g in the 0.1 M $NaNO_2$ -0.1 M HNO_3 solution, nearly 15 times more than that in the 0.1 M HNO_3 solution. The pseudo-second-order kinetic model and the Langmuir isotherm equation are suitable for expressing the adsorption characters of Ru(III) on SiPyR-N3, in which the adsorption process is endothermic. SiPyR-N3 has good adsorption ability and selectivity of about 100 for Ru in simulated HLLW with $SF_{Ru/other \text{ metal ions}}$, except for Zr, in 0.1 M $NaNO_2$ -0.1 M HNO_3 solution. The adsorption mechanism involves the complexation of the pyridine functional group (C-N=C) with $Ru(NO)^{3+}$ and its complexes with NO_2^- and NO_3^- , as well as the anion exchange mechanism between protonated amine in SiPyR-N3 and Ru complex anionic species. Furthermore, Ru could be effectively desorbed by 0.1 M $HNO_3 + 1$ M thiourea, and the desorption rate reached 92% at 328 K, which increased with increasing temperature.

Supplementary Materials: The following supporting information can be downloaded at: <https://www.mdpi.com/article/10.3390/toxics12030181/s1>, Table S1: Kinetic parameters of SiPyR-N3 adsorption of Ru in nitric acid system in nitric acid–nitrite system at 298, 308, and 318 K; Table S2: The adsorption isotherm parameters of two adsorption models for Ru on SiPyR-N3 in two systems at 298, 308, and 318 K; Table S3: Thermodynamic parameters of Ru adsorption on SiPyR-N3 in nitric acid system and in nitric acid–nitrite system; Figure S1: Effect of initial $NaNO_2$ concentration on adsorption. ($m/V = 0.02 \text{ g mL}^{-1}$, $C_{Ru} = 2 \text{ mmol L}^{-1}$, $C_{HNO_3} = 0.1 \text{ mol L}^{-1}$, $T = 298 \text{ K}$); Figure S2: Effect of initial HNO_3 concentration on adsorption. ($m/V = 0.02 \text{ g mL}^{-1}$, $C_{Ru} = 2 \text{ mmol L}^{-1}$, $T = 298 \text{ K}$).

Author Contributions: Conceptualization, Y.W.; methodology, Y.W. and T.J.; writing—review and editing, C.X. and S.N.; writing—original draft preparation, C.L. (Cong Li) and T.J.; investigation and data curation, C.L. (Cong Li), L.C., Q.Z. and J.W.; supervision, Y.W., C.L. (Caiwu Luo) and L.C.; project administration, Y.W. and S.N. All authors have read and agreed to the published version of the manuscript.

Funding: This research was financially supported by the National Natural Science Foundation of China (Grant No. 11975082, 22066005, 22350710186, and U23B20167), the Hunan Provincial Natural Science Foundation of China (Grant No. 2022JJ50152, 2022JJ50156), the Scientific Research Fund of Hunan Provincial Education Department (Grant No. 21B0413, 22A0315), and the open foundation of National Isotope Engineering Technology Research Center (GJTWSGCZX-202302).

Institutional Review Board Statement: Not applicable.

Informed Consent Statement: Not applicable.

Data Availability Statement: The data presented in this study are available on request from the corresponding author.

Conflicts of Interest: The present research work carries no conflicts of interest.

References

1. Liu, L.; Guo, H.; Dai, L.; Liu, M.; Xiao, Y.; Cong, T.; Gu, H. The role of nuclear energy in the carbon neutrality goal. *Prog. Nucl. Energy* **2023**, *162*, 104772. [[CrossRef](#)]
2. Xiao, Y. The relationship between the development of nuclear power in China and the storage and post-treatment of spent fuel. *Electr. Eng.* **2020**, *18*, 24–25+57.
3. Zhang, S. Preparation of Silica-Based Composite Functional Materials and Study on Its Adsorption and Separation Behavior of Ruthenium Rhodium, and Palladium. Master's Thesis, Guangxi University, Nanning, China, 2021. [[CrossRef](#)]
4. Verma, P.K.; Mohapatra, P.K. Ruthenium speciation in radioactive wastes and state-of-the-art strategies for its recovery: A review. *Sep. Purif. Technol.* **2021**, *275*, 119148. [[CrossRef](#)]
5. Moeyaert, P.; Miguirditchian, M.; Masson, M.; Dinh, B.; Hérès, X.; De Sio, S.; Sorel, C. Experimental and modelling study of ruthenium extraction with tri-n-butylphosphate in the purex process. *Chem. Eng. Sci.* **2017**, *158*, 580–586. [[CrossRef](#)]
6. Wu, H.; Kim, S.-Y.; Takahashi, T.; Oosugi, H.; Ito, T.; Kanie, K. Extraction behaviors of platinum group metals in simulated high-level liquid waste by a hydrophobic ionic liquid bearing an amino moiety. *Nucl. Eng. Technol.* **2021**, *53*, 1218–1223. [[CrossRef](#)]
7. Swain, P.; Mallika, C.; Srinivasan, R.; Mudali, U.K.; Natarajan, R. Separation and recovery of ruthenium: A review. *J. Radioanal. Nucl. Chem.* **2013**, *298*, 781–796. [[CrossRef](#)]
8. Li, F.; Shang, Y.; Ding, Z.; Weng, H.; Xiao, J.; Lin, M. Efficient extraction and separation of palladium (Pd) and ruthenium (Ru) from simulated HLLW by photoreduction. *Sep. Purif. Technol.* **2017**, *182*, 9–18. [[CrossRef](#)]
9. Rzelewska-Piekut, M.; Wisniewski, M.; Regel-Rosocka, M. Effect of composition and ageing of chloride solutions on extraction of Rh(III) and Ru(III) with phosphonium ionic liquids Cyphos IL 101 and IL 104. *Sep. Sci. Technol.* **2017**, *53*, 1249–1260. [[CrossRef](#)]
10. Verma, P.K.; Mohapatra, P.K. Highly efficient separation of ruthenium from alkaline radioactive feeds using an anion exchange resin. *Radiochim. Acta* **2020**, *108*, 603–613. [[CrossRef](#)]
11. Vereecken, P.M.; Radisic, A.; Ross, F.M. Differential Inhibition during Cu Electrodeposition on Ru: Combined Electrochemical and Real-Time TEM Studies. *J. Electrochem. Soc.* **2019**, *166*, D3129. [[CrossRef](#)]
12. Song, Y.; Tsuchida, Y.; Matsumiya, M.; Tsunashima, K. Recovery of ruthenium by solvent extraction and direct electrodeposition using ionic liquid solution. *Hydrometallurgy* **2018**, *181*, 164–168. [[CrossRef](#)]
13. Swain, P.; Mallika, C.; Jagadeeswara Rao, C.; Kamachi Mudali, U.; Natarajan, R. Electrochemical studies on the reduction behaviour of ruthenium nitrosyl ions in nitric acid medium. *J. Appl. Electrochem.* **2015**, *45*, 209–216. [[CrossRef](#)]
14. Reddy, S.R.; Pandey, N.K.; Mallika, C.; Mudali, U.K. Equilibrium and kinetics of adsorption of ruthenium on activated charcoal from nitric acid solutions. *Chem. Eng. Res. Des.* **2016**, *115*, 91–97. [[CrossRef](#)]
15. Ito, T.; Nagaishi, R.; Kimura, T.; Kim, S.-Y. Study on radiation effects on (MOTDGA–TOA)/SiO₂-P adsorbent for separation of platinum group metals from high-level radioactive waste. *J. Radioanal. Nucl. Chem.* **2015**, *305*, 419–427. [[CrossRef](#)]
16. Mohanty, B.; Yuvaraj, R.; Jena, H.; Ponraju, D. Graphene Oxide as an Adsorbent for Ruthenium from Aqueous Solution. *ChemistrySelect* **2022**, *7*, e202200078. [[CrossRef](#)]
17. Lee, S.H.; Chung, H. Ion Exchange Characteristics of Palladium and Ruthenium from a Simulated Radioactive Liquid Waste. *Sep. Sci. Technol.* **2003**, *38*, 3459–3472. [[CrossRef](#)]
18. Suzuki, T.; Morita, K.; Sasaki, Y.; Matsumura, T. Separation of Ru(III), Rh(III) and Pd(II) from Nitric Acid Solutions Using Ion-Exchange Resins Bearing Carboxylic Betaine. *Sep. Sci. Technol.* **2016**, *51*, 2815–2822. [[CrossRef](#)]
19. Zhang, W.; Zhu, H.; Liu, S.-f.; Ning, S.; Wei, Y.-z. Scandium recovery from ion-adsorption rare earth concentrate with HEHEHP as extractant. *J. Cent. South Univ.* **2021**, *28*, 679–689. [[CrossRef](#)]
20. Ning, S.; Zhang, S.; Zhang, W.; Zhou, J.; Wang, S.; Wang, X.; Wei, Y. Separation and recovery of Rh, Ru and Pd from nitrate solution with a silica-based IsoBu-BTP/SiO₂-P adsorbent. *Hydrometallurgy* **2020**, *191*, 105207. [[CrossRef](#)]
21. Dumas, T. Coupling Raman spectroscopy and DFT study for enhanced description of nitrosyl nitrate ruthenium(III) complexes in nitric acid. *J. Radioanal. Nucl. Chem.* **2020**, *326*, 1213–1223.
22. Zhang, A.; Wei, Y.; Arai, T.; Kumagai, M. Palladium Removal from the Simulated Nuclear Spent Fuel Solution Using a Silica-Based SiPyR-N3 Anion Exchanger. *Solvent Extr. Ion Exch.* **2006**, *24*, 447–462. [[CrossRef](#)]
23. Chen, Y. Study on Synthesis of Silica Based Anion Exchange Resin and Their Application in Thorium Based Spent Fuel Reprocessing. Doctoral Dissertation, Shanghai Jiaotong University, Shanghai, China, 2017.
24. Brown, P.G.M. Nitro complexes of nitrosylruthenium. *J. Inorg. Nucl. Chem.* **1960**, *13*, 73–83. [[CrossRef](#)]
25. Emel'yanov, V. The state of ruthenium in nitrite-nitrate nitric acid solutions as probed by NMR. *Russ. J. Inorg. Chem.* **2006**, *51*, 1811–1819. [[CrossRef](#)]
26. Donat, R.; Aytas, S. Adsorption and Thermodynamic Behavior of Uranium(VI) on Ulva sp.-Na Bentonite Composite Adsorbent. *J. Radioanal. Nucl. Chem.* **2005**, *265*, 107–114. [[CrossRef](#)]
27. Hu, Y.; Guo, T.; Xia, F.; Wang, Z.; Wang, W.; Wang, Y.; Ma, S. Phosphorus-zirconium co-doped walnut shell biochar prepared by pyrolysis for efficient Pb (II) captured from synthetic wastewater. *J. Environ. Chem. Eng.* **2023**, *11*, 110964. [[CrossRef](#)]

28. Donat, R.; Esen Erden, K.; Cetisli, H.; Aytas, S. Adsorption of Uranium(VI) onto *Ulva* sp.-Sepiolite Composite. *J. Radioanal. Nucl. Chem.—J Radioanal. Nucl. Chem.* **2009**, *279*, 253–261. [[CrossRef](#)]
29. Sert, Ş.; Kütahyalı, C.; İnan, S.; Talip, Z.; Çetinkaya, B.; Eral, M. Biosorption of lanthanum and cerium from aqueous solutions by *Platanus orientalis* leaf powder. *Hydrometallurgy* **2008**, *90*, 13–18. [[CrossRef](#)]
30. Das, A.; Chandrakumar, K.R.S.; Paul, B.; Chopade, S.M.; Majumdar, S.; Singh, A.K.; Kain, V. Enhanced adsorption and separation of zirconium and hafnium under mild conditions by phosphoric acid based ligand functionalized silica gels: Insights from experimental and theoretical investigations. *Sep. Purif. Technol.* **2020**, *239*, 116518. [[CrossRef](#)]
31. Yang, Y.; Yang, Y.; He, C.; Wei, Y.; Fujita, T.; Wei, Z.; Yang, Y.; Shen, F. The adsorption and desorption behavior and mechanism research of cobalt, nickel and copper in nitrite—Sulfuric acid system. *Sep. Sci. Technol.* **2022**, *57*, 1848–1859. [[CrossRef](#)]
32. Hamza, M.F.; Abd El-Hamid, A.A.M.; Guibal, E.; Abdel-Rahman, A.A.H.; El Araby, R. Synthesis of a new pyrimidine-based sorbent for indium(III) removal from aqueous solutions—Application to ore leachate. *Sep. Purif. Technol.* **2023**, *314*, 123514. [[CrossRef](#)]
33. Liu, H.; Tuerxun, A.; Liu, X.; Ruxianguli, J.; Zou, D.; Tang, X. Preparation of Novel Donor Acceptor Conjugated Polymer/TiO₂ Composite Containing Pyridine Unit and Its Application in UV Photodetectors. *J. Xinjiang Univ.* **2023**, *40*, 320–330+366.
34. Rabchinskii, M.K.; Ryzhkov, S.A.; Kirilenko, D.A.; Ulin, N.V.; Baidakova, M.V.; Shnitov, V.V.; Pavlov, S.I.; Chumakov, R.G.; Stolyarova, D.Y.; Besedina, N.A.; et al. From graphene oxide towards aminated graphene: Facile synthesis, its structure and electronic properties. *Sci. Rep.* **2020**, *10*, 6902. [[CrossRef](#)] [[PubMed](#)]
35. Zhao, S.; Zhang, Y.; Zhou, Y.; Wang, Y.; Qiu, K.; Zhang, C.; Fang, J.; Sheng, X. Facile one-step synthesis of hollow mesoporous g-C₃N₄ spheres with ultrathin nanosheets for photoredox water splitting. *Carbon* **2018**, *126*, 247–256. [[CrossRef](#)]
36. Zhu, H.; Lin, W.; Li, Q.; Hu, Y.; Guo, S.; Wang, C.; Yan, F. Bipyridinium-Based Ionic Covalent Triazine Frameworks for CO₂, SO₂, and NO Capture. *ACS Appl. Mater. Interfaces* **2020**, *12*, 8614–8621. [[CrossRef](#)]
37. Duan, X. Preparation of Pyridine-Based Porous Organic Framework and Their Catalytic Properties for CO₂ Cycloaddition Reaction. Master's Thesis, Qingdao University of Science and Technology, Qingdao, China, 2023.

Disclaimer/Publisher's Note: The statements, opinions and data contained in all publications are solely those of the individual author(s) and contributor(s) and not of MDPI and/or the editor(s). MDPI and/or the editor(s) disclaim responsibility for any injury to people or property resulting from any ideas, methods, instructions or products referred to in the content.